

Nucleation and solidification in static arrays of monodisperse drops†

Jon F. Edd,^a Katherine J. Humphry,^b Daniel Irimia,^a David A. Weitz^{bc} and Mehmet Toner^{*a}

Received 4th December 2008, Accepted 12th March 2009

First published as an Advance Article on the web 3rd April 2009

DOI: 10.1039/b821785h

The precise measurement of nucleation and non-equilibrium solidification are vital to fields as diverse as atmospheric science, food processing, cryopreservation and metallurgy. The emulsion technique, where the phase under study is partitioned into many droplets suspended within an immiscible continuous phase, is a powerful method for uncovering rates of nucleation and dynamics of phase changes as it isolates nucleation events to single droplets. However, averaging the behavior of many drops in a bulk emulsion leads to the loss of any drop-specific information, and drop polydispersity clouds the analysis. Here we adapt a microfluidic technique for trapping monodisperse drops in planar arrays to characterize solidification of highly supercooled aqueous solutions of glycerol. This system measured rates of nucleation between 10^{-5} and 10^{-2} $\text{pL}^{-1} \text{s}^{-1}$, yielded an ice-water interfacial energy of 33.4 mJ m^{-2} between -38 and -35 °C, and enabled the specific dynamics of solidification to be observed for over a hundred drops in parallel without any loss of specificity. In addition to the physical insights gained, the ability to observe the time and temperature of nucleation and subsequent growth of the solid phase in static arrays of uniform drops provides a powerful tool to discover thermodynamic protocols that generate desirable crystal structures.

Introduction

Although solidification from the melt is favorable at temperatures below the equilibrium melting point (T_m), some supercooling typically occurs before a stable solid nucleus forms. This is because the positive Gibbs free energy associated with the solid–liquid interface inhibits solidification until a critical number of liquid molecules have arranged stochastically into the correct packing of the solid phase and then gain an additional molecule. From the point of nucleation onwards, the negative Gibbs free energy of phase change drives the system towards the equilibrium solid state. The rate of homogeneous nucleation (J , in $\text{m}^{-3} \text{s}^{-1}$) is defined as the average number of stable solid nuclei that are produced during an increment of time and within a defined volume of the super-cooled fluid, without the aid of surface- or impurity-mediated (heterogeneous) nucleation.

At the atomic level, local thermal fluctuations constantly lead to spontaneous formation of crystal-like nuclei of various sizes and structures. Besides comparatively rare multi-molecule additions to or losses from such groupings, molecular monomers of fluid then attach or detach with rates that depend on temperature and pressure.¹ Over time, sub-critical nuclei will tend to melt and super-critical nuclei will grow until equilibrium is reached. The forward and reverse reaction rates in each step of this chain reaction, from single molecule to super-critical nucleus, will affect

the overall rate of nucleation; however, one can simplify the problem considerably by focusing on the most critical step: the addition of one fluid molecule to a critically-sized nucleus, while ignoring all others. From nucleation theory,^{2–4} J can then be expressed as the product of a Boltzmann distribution, indicating the relative abundance of critically-sized nuclei,⁵ and an expression that predicts how often these nuclei incorporate another fluid molecule⁶—this second factor is sometimes given instead as the monomer attachment frequency times the Zeldovich factor.⁷ The rate of homogeneous nucleation is then:

$$J = \eta \exp\left(-\frac{\Delta G}{kT}\right) \frac{kT}{h} \exp\left(-\frac{\Delta g}{kT}\right) \quad (1)$$

where η is the number of fluid molecules per unit volume, ΔG is the free energy of a nucleus of critical size, k is the Boltzmann constant, T is the absolute temperature of the liquid, h is Planck's constant and Δg is the free energy change associated with the transfer of an additional molecule to the critical-size nucleus. As homogeneous nucleation is a stochastic process in both time and space, the probability of k nucleation events inside a liquid volume V , and during a time t in which J is unchanging (constant supersaturation), follows a Poisson distribution:

$$P_m = (tVJ)^m \exp(-tVJ)/(m!) \quad (2)$$

Precise measurement of the intrinsic homogeneous nucleation rate is a window into non-equilibrium thermodynamics on the scale of atoms and molecules, yielding fundamental physical insights that have practical implications for fields as diverse as atmospheric science,^{8,9} food processing,¹⁰ protein crystallization,^{11,12} cryopreservation^{13,14} and metallurgy.¹⁵ However, nucleation rates are difficult to predict with accuracy as small errors in the assumed values for the temperature-dependent quantities ΔG and Δg lead to exponentially different values of J .

^aCenter for Engineering in Medicine, BioMEMS Resource Center, Massachusetts General Hospital, Harvard Medical School, Shriners Hospital for Children, Boston, MA, USA. E-mail: mehmet_toner@hms.harvard.edu

^bDepartment of Physics, Harvard University, Cambridge, MA, USA

^cSchool of Engineering and Applied Sciences, Harvard University, Cambridge, MA, USA

† Electronic supplementary information (ESI) available: Five video files, description of videos, mask file, data file. See DOI: 10.1039/b821785h

Consequently, homogeneous nucleation rates must be experimentally measured if there is to be confidence in the resulting insights. Heterogeneous nucleation, which refers to the growth of the solid phase from the surface of another material, usually a particle, precedes homogeneous nucleation unless the contiguous fluid volume does not contain particulate impurities. Even subtle heterogeneous nucleation can increase the apparent nucleation rates substantially. Reducing the volume of the observed fluid decreases the probability a particulate impurity is present. This consideration led to the development of the emulsion technique,^{16–19} where the studied fluid is dispersed into many drops suspended in an immiscible continuous phase such as oil, preventing each nucleation event, whether homogeneous or heterogeneous, from solidifying more than a single drop. Moreover, the emulsion technique isolates any impurities within a finite number of droplets, and if drop volume is small when compared to the average fluid volume per nucleating particle, most drops will nucleate homogeneously. While the statistical advantage derived from averaging the behavior of a large numbers of drops is remarkable, the technique has been limited by the polydispersity of the measured emulsions¹⁸ as solidification of a large drop will influence the measured rate of nucleation more than that of a small drop. In practice, this uncertainty is limited by measuring the size distribution of the drops and then making an assumption, for instance that large drops will always solidify before smaller drops.²⁰ Other approaches include the observation of individual drops of known volume as they freeze²¹ or the measurement of the fraction of uniformly-sized drops that have frozen after being super-cooled for a fixed time and at a specific temperature.^{17,22,23} These techniques make no assumptions about the volume-dependence of nucleation, but suffer from a lower statistical power and higher experimental burden in the first case, and a loss of drop-specific history in the second case.

Here, we generate and trap monodisperse drops²⁴ in a recently described static microfluidic array,²⁵ enabling the measurement of nucleation kinetics (see ref. 26 for a recent review of such lab-on-a-chip methods) in bulk emulsions without assumptions regarding the volume-dependence of nucleation. Instead of utilizing robotic techniques for arraying droplets of 100 nL and larger volume,²⁷ we achieve this in a microfluidic system that allows for the simultaneous observation of nucleation events within more than one hundred uniformly-sized (picolitre-scale) and immobilized aqueous drops during one or more cooling cycles. In addition to the inherent benefits of drop monodispersity, the technique presented here allows for the expansion of the study of non-equilibrium solidification in a manner that is conducive to a deeper understanding of the stochastic nature of nucleation than is possible from observing the liquid-solid phase transition of many drops collectively. More specifically, the experiment has been designed so that the precise time and temperature at the completion of freezing within each individual drop can be observed during a controlled thermal excursion below the equilibrium freezing point of the disperse phase under study, here aqueous solutions of glycerol. Since the formation of a stable crystal nucleus within any particular super-cooled liquid is posited to occur at random with a certain frequency that scales linearly with the available liquid volume at a given thermodynamic state, the concurrent observation of drop volume and time of freezing completely separates time-stochasticity from polydispersity artifacts that together influence the observed nucleation rates in bulk emulsions.

Materials and methods

Experiment

The physical embodiment of this concept is depicted in Fig. 1. A temperature controlled microscope stage is combined with optical recording of a monolayer of drops trapped in

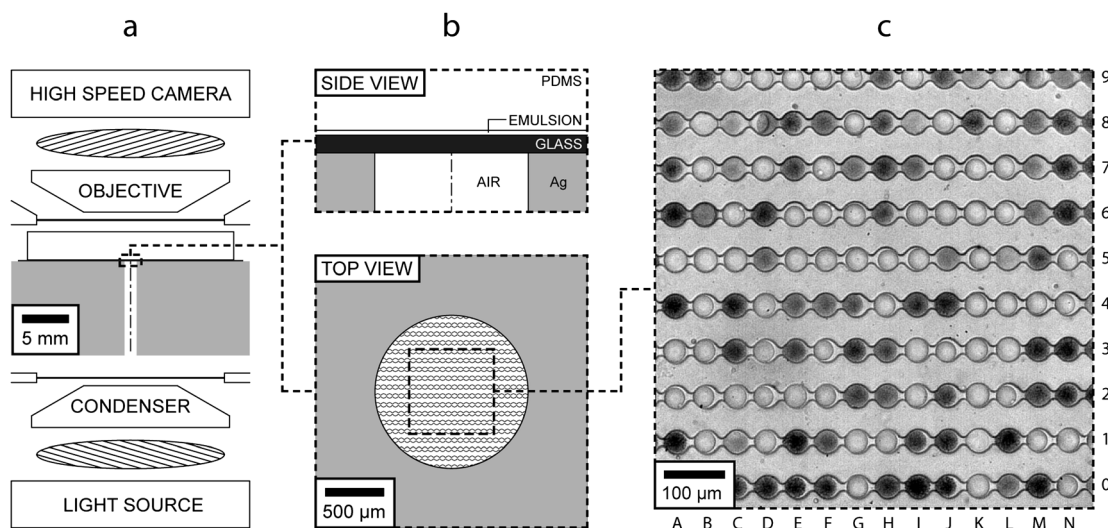


Fig. 1 Experimental apparatus for observing nucleation within monodisperse microdrops. Drops are kept at controlled temperature with the system in (a), where the microfluidic device sits on an enclosed cryostage. Magnified side and top views along the optical path are given in (b), where trapped drops, 10% w/w glycerol in water for this case, were imaged as in (c). Video recordings of the sample cooling *via* cross-polarization microscopy resolved nucleation times precisely within each drop due to the associated jump discontinuity in volume, brief flashing when viewed with crossed polarizers and delayed darkening post-freezing. The drop in L3 is unfrozen, while the drop to its immediate right (M3) has been frozen for several seconds during which it has darkened considerably. The drop in K1 has just frozen. Reservoir at D8 contains one frozen (right) and one unfrozen (left) drop.

a microfluidic device that sits on the cold stage and in the optical path of the microscope.

Monodisperse drops of identical composition (aqueous solutions with 0, 10, 20 and 30% w/w glycerol were explored) are generated with a technique described elsewhere.²⁴ Drop formation is extremely stable over a wide range of flow rates for the aqueous and oil phases,²⁸ allowing thousands of drops to be generated per second from a single nozzle with the drop diameter typically varying by less than 2% in the resulting emulsion.²⁹ The network of microfluidic channels used to generate monodisperse drops includes a 41 μm -thick rectangular array of drop traps (see Fig. 1C and supplementary mask file in the ESI†, where traps are spaced by 50 μm within individual channels and by 75 μm across parallel channels) downstream from the drop-generating nozzle.²⁵ By tuning flow rates (PHD 2000; Harvard Apparatus, Holliston, MA) to match the drop size to the size of the traps, the regular array is filled with surfactant-stabilized (PFPE-PEG block copolymer) drops³⁰ suspended in a continuous fluorocarbon oil phase (FC-40; 3M, St. Paul, MN). This device allows drops to be immobilized and separated by a prescribed distance so that the behavior of individual drops can be tracked throughout experiments.

Microfluidic devices are manufactured with standard soft lithography techniques.³¹ Specifically, channels in polydimethylsiloxane (PDMS) are bonded *via* oxygen plasma to #1 cover glass. To ensure that the fluorinated oil preferentially wets all four walls of the microchannels, a hydrophobic coating is applied to the channel walls by pushing a small amount of Aquapel (PPG Industries, Pittsburgh, PA), followed immediately by ~ 1 ml of air, through the network of microchannels.

The microfluidic device containing trapped monodisperse drops is then placed on the controlled-temperature silver block of a cryostage (FDCS196; Linkam Scientific Instruments Ltd, UK). To prevent excessive frost formation obscuring the microscope light path, the surrounding pressure chamber is closed, but kept at atmospheric pressure. After the cryostage stabilized to a temperature above that where homogeneous nucleation rates are significant, a constant cooling rate of 0.01 $^{\circ}\text{C/s}$ is applied to the cryostage *via* software (Linksys 32, Linkam). A Phantom v4.2 camera (Vision Research, Wayne, NJ) is used to record a microscopic video that captures all nucleation events with exactly 1000 video frames for each degree Celsius drop in temperature. The cryostage temperature is recorded every 300 ms and the resulting data file is synchronized manually to the corresponding image sequence with an error of not more than one second.

Although this implies a synchronization precision of 0.01 $^{\circ}\text{C}$, a lag in temperature of the microfluidic device with respect to the cryostage must be taken into account. Numerical models of heat diffusion in this system (Comsol; Comsol AS, Stockholm, Sweden) indicate this thermal lag is between 0.1 $^{\circ}\text{C}$ and 1 $^{\circ}\text{C}$ for our experiments. Briefly, this was a 2D model of transient heat diffusion with cylindrical symmetry about the centerline drawn in Fig. 1a. The model domain was bounded by a rectangle of width equal to 12.7 mm (cryostage silver block radius) and height equal to 4.7 mm (distance between the upper surface of the cryostage silver block and the upper surface of the glass lid enclosing the chamber). From bottom to top, this model contained a 150 μm -thick cover glass, 3.9 mm of PDMS, 450 μm of air and a second 200 μm -thick layer of glass (enclosure lid). The

initial condition was set to ambient temperature everywhere within the geometry (20 $^{\circ}\text{C}$). Along the lower edge of the model (the cryostage surface), a temperature boundary condition was imposed to enforce a 0.01 $^{\circ}\text{C s}^{-1}$ cooling ramp from ambient to -80 $^{\circ}\text{C}$, except that the first 650 μm from the centerline (hole in the silver block for the optical path) was set to thermal insulation. Finally, the upper surface of glass was set to ambient temperature and all other boundaries (centerline and the $r = 12.7$ mm edge) were set to thermal insulation. However, the measured thermal lag between an insulated T-type thermocouple made from 80 μm -diameter wires (5TC; Omega Engineering, Stamford, CT) placed at the intersection of the axis of symmetry in Fig. 1 with the glass-PDMS boundary, where drops reside during a cooling protocol, and the temperature sensor inside the cryostage is somewhat larger than that predicted by modeling. If we model the thermal circuit as two thermal resistances in series, where the cryostage temperature and measured temperature bound the first resistance, and the same measured temperature and room temperature bound the second resistance, we find the thermal behavior to be well approximated ($R^2 = 0.999$) as $(T - 20$ $^{\circ}\text{C}) = 0.959 (T_{\text{cs}} - 20$ $^{\circ}\text{C})$, where T_{cs} is the cryostage temperature (x-axis in Fig. 2) and T is the actual temperature near the drop array. This results in a lag of 2.4, 2.5, 2.8 and 3.2 $^{\circ}\text{C}$ when T_{cs} is -37.6 , -42.0 , -49.3 and -59.2 $^{\circ}\text{C}$ respectively (the center temperatures for 0, 10, 20 and 30% w/w glycerol in water experiments). When this upper bound (the thermocouple is thicker than the drop array and in poor thermal contact with the cover glass) on the thermal lag is taken into account, our measured values of J for pure water (in Fig. 2) compare favorably with other reported results.³² Moreover, the rapid change in nucleation rates that often occurs over narrow ranges in temperature underscores the need for precise control of sample temperature; here, an error of only 1 $^{\circ}\text{C}$ in sample temperature would correspond with around an order of magnitude error in J .

During cooling, it is possible to observe solidification of individual drops in at least two of three different ways. Most reliable is the 9.07% increase in volume that occurs when water freezes at 0 $^{\circ}\text{C}$,³³ evident as a sudden small expansion of the drop diameter (see Fig. 3 and ESI video 5†), and often occurring within a single frame. Additionally, freezing is followed by a somewhat delayed but obvious darkening of the drop under both crossed-polarizers and phase contrast microscopy. Finally, for water drops observed through crossed-polarizers, drop crystallization causes the sudden appearance of an alternating light and dark pattern on an otherwise dark field. This occurs because the incoming plane-polarized light traveling through a frozen drop is distorted by the birefringent properties of water-ice so that the second (orthogonal) polarizer no longer prevents all transmitted light from reaching the camera. For mixtures of water and glycerol viewed through crossed-polarizers, a bright flash occurs within the freezing drop (see Fig. 3). This is probably due to the overlapping time scales of the initial crystallization and the subsequent overall darkening.

The freezing times for individual drops are measured with full temporal resolution from the resulting image sequences. Drop diameters are measured manually three times (ImageJ; NIH, USA) from the image immediately preceding freezing, a measurement that is possible as the oil-water boundary is

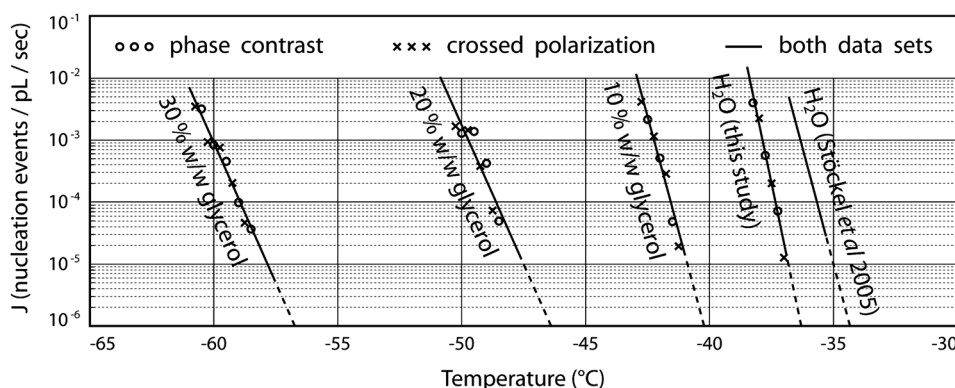


Fig. 2 Recovered rates of nucleation. Freezing of around 100 monodisperse microdrops trapped within an array (see Fig. 1c) was observed *via* phase contrast microscopy, then with the method of crossed polarizers, during two identical constant cooling protocols ($-0.01\text{ }^{\circ}\text{C s}^{-1}$). The number of nucleation events per picolitre per second (J) was recovered from these recorded freezing events (time and temperature for each microdrop) by maximizing the likelihood function in eqn (6), where J was modeled as in eqn (7).

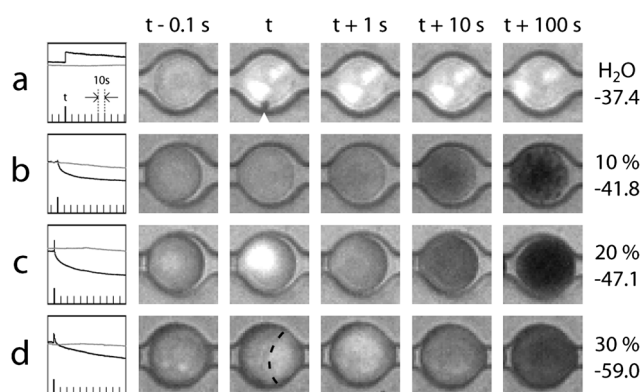


Fig. 3 Dynamics of drops before and after nucleation. Images in rows (a)–(d) resulted from a drop with 0, 10, 20 or 30% w/w glycerol in water. Freezing was first observed in the second column of images, at time t and a temperature marked to the right of each row (in $^{\circ}\text{C}$). All crossed-polarization micrographs are $50\text{ }\mu\text{m}$ squares. Two curves at left for each case depict the dynamics of mean drop brightness within a 2 minute window (ten second grid, time t in bold), for the imaged drop (black) and for the entire array (gray). Temperature falls by $1\text{ }^{\circ}\text{C}$ every 100 s. Note the small air bubble expelled during freezing in (a), marked with an arrow, and solid–liquid interface in (d) at time t . ESI movies† 1 through 4 show the entire area of imaged drop-array from one second before to ten seconds after the nucleation events depicted in (a)–(d) respectively.

always visible due to the mismatch in refractive indices between the two phases.

Recovery of nucleation rates

Given the individual volumes and freezing times for a population of chemically identical drops that embark upon a prescribed cooling cycle, it is possible to deduce how frequently ice embryos of critical size are formed as a function of time, which taken together with the measured time-course of cryostage temperature, reveals the nucleation rate in the disperse phase under study, across the temperature range where drops freeze. In the following theoretical development, it is important to note the implicit assumption that nucleation is homogeneous. Moreover,

though we filtered all fluids ($0.2\text{ }\mu\text{m}$ pore size), we cannot rule out the presence of smaller heterogeneous nucleating particles that are abundant enough to cause rates of nucleation to appear higher¹⁶ than the true values.

In the simplest experiment, drops are held at constant temperature, incurring a constant rate of nucleation per unit volume (J), until all drops have frozen. In this case, the probability that the first nucleation event within a drop of volume V occurs before t seconds have elapsed is described by a modified Poisson distribution, such that

$$P_{\hat{\tau} < t} = 1 - P_{\hat{\tau} \geq t} = 1 - \exp(-tVJ) = \int \tau dt \quad (3)$$

where τ is the probability density function for the time to the first nucleation event within the drop ($\hat{\tau}$). By differentiating with respect to t , we obtain:

$$\tau = VJ \exp(-tVJ) \quad (4)$$

In order to estimate J from a set of measured times to nucleation ($\hat{\tau}$) in n drops, we can then define the following likelihood function:

$$L(J) = \prod_{i=1}^n \tau(\hat{\tau}_i) = \prod_{i=1}^n V_i J \exp(-\hat{\tau}_i V_i J) \quad (5)$$

By maximizing L with respect to J we obtain the maximum likelihood estimate for J given the observed freezing times and drop volumes, from which it follows that the rate of stable nuclei formation per volume (J) is $1/\tau_m V$, where τ_m is the mean time to freezing for n monodisperse drops.

However, this type of experiment limits the range of accessible temperatures and time scales. For example, it is difficult to rapidly cool a sample of emulsion without incurring small oscillations about the target temperature that violate the assumption of uniform thermal conditions. This is not an issue if the mean freezing time is much longer than the time to thermal stabilization or if the oscillations are small enough to have little effect on J , but it will prevent accurate recovery of J for lower temperatures where nucleation rates are much higher and even small oscillations lead to large differences in J .

To overcome this shortcoming and to allow for the recovery of nucleation rates at different temperatures within a single experiment, we chose instead to set a constant cooling rate. Since J will then vary during the course of the experiment, eqn (3) must be modified so that the quantity $-tVJ$ is replaced with the integral of $-VJ(t)$ up to t . As a result, the likelihood function becomes

$$L(J(t)) = \prod_{i=1}^n V_i J(\hat{\tau}_i) \exp \left(-V_i \int_{-\infty}^{\hat{\tau}_i} J(t) dt \right) \quad (6)$$

To find the maximum likelihood estimate for $J(t)$ it is then desirable to specify a particular functional form for J such that the governing parameters can be extracted *via* numerical optimization. Since J has been reported to increase exponentially as one approaches the so-called homogeneous nucleation temperature³⁴ we chose the following functional form:

$$J(t) = \exp \left[\frac{\ln(J_{i+1}) - \ln(J_i)}{t_{i+1} - t_i} (t - t_i) + \ln(J_i) \right] = J_i \left(\frac{J_{i+1}}{J_i} \right)^{\frac{t-t_i}{t_{i+1}-t_i}} \quad (7)$$

Here, J_i represent the recovered nucleation rates for a set of N chosen times during an experiment, resulting in a piecewise-linear variation of $\ln(J)$ with t , and hence with $-T$, in N minus one intervals. This also allows the integral in eqn (6) to be easily computed for any particular choice of J_i . We then maximize L as a function of J_i though J_N , yielding the maximum likelihood estimate for $J(t)$ and thus $J(T)$, valid from the start of the experiment up to the time when the last drop was observed to freeze.

Results and discussion

Recovered from the raw data in the ESI spreadsheet file†, rates of nucleation are reported in Fig. 2 for each of four concentrations of glycerol in water (0, 10, 20 and 30% w/w). The two sets of marked points for each concentration represent the values of J_i to J_N that appear in eqn (7), during a cooling protocol performed on an array of drops, viewed first with phase contrast (circles) and then with crossed polarization microscopy (crosses). Solid curves show the result of combining both data sets (more than 200 nucleation events) for a given glycerol mass fraction and finding the linear fit of $\log(J)$ vs. T , yielding the maximum likelihood estimate according to eqn (6). Respectively, the slope ($\partial \log J / \partial T$) and intercept ($\log J_0$ °C in $\text{pL}^{-1} \text{s}^{-1}$), are $-1.912/^\circ\text{C}$ and -75.4 for the 0% line, $-1.476/^\circ\text{C}$ and -65.4 for 10%, $-0.896/^\circ\text{C}$ and -47.6 for 20% and $-0.902/^\circ\text{C}$ and -57.2 for 30% w/w glycerol in DIW. These lines are solid in the temperature interval during which drops were observed to freeze, although according to eqn (6) the curves are valid for earlier times as well (dashed lines). The slope and intercept for a reference curve for water³² were found to be $-1.468/^\circ\text{C}$ and -56.1 respectively ($R^2 = 0.935$, data was extracted manually from Fig. 6 of the cited work). Alternatively, by fitting our data on water as $J = Q \exp(\kappa \Delta T^{-2} T^{-3})$,⁵ where ΔT is super-cooling, we obtain $Q = 1.3 \times 10^{59} \text{ m}^{-3} \text{ s}^{-1}$ and $\kappa = -2.0 \times 10^{12} \text{ K}^5$ ($R^2 = 0.998$). Compare these to the values derived from the reference curve in Fig. 2 (Stöckel *et al.*³²): $Q = 9.8 \times 10^{45} \text{ m}^{-3} \text{ s}^{-1}$ and $\kappa = -1.4 \times 10^{12} \text{ K}^5$ ($R^2 = 0.936$).

To ensure unique nucleation events, we then considered drop-to-drop propagation of crystallization. This could occur if two drops were touching and the ice physically breached the immiscible gap of oil or possibly *via* the brief shock wave associated with the rapid expansion associated with freezing, though larger increases in pressure could hinder solidification.³⁵ For the recovery of nucleation rates from the freezing of bulk emulsions, this would be particularly problematic, resulting in higher apparent rates of nucleation. To ensure no drop-to-drop propagation of crystallization occurred in our experiments, we took advantage of the recorded spatial and temporal resolution of each nucleation event. We analyzed sequences of nucleation events to see if their temporal separation was too small to be easily explained by the overall rate of nucleation recovered from the experiment. The microfluidic array that we employed prevents direct contact of drops, but even in cases where two drops filled the same reservoir, we observe no propagation across the narrow gap of oil (D8 of Fig. 1c).

By comparing the reference curve for water with our data, there is an apparent difference in the temperature for which a particular nucleation rate occurs; specifically, our data for water crosses $10^{-3} \text{ pL}^{-1} \text{ s}^{-1}$ at a temperature that is 1.4°C colder than for the reference data. Previous results fall within a $\pm 1^\circ\text{C}$ band centered on the reference curve adopted here, and since it is likely that our system incurred a small thermal lag between the measured temperature in the cryostage silver block and the actual temperature in the droplets within the array, our data is consistent with the reference curve for water. In addition, by performing a linear regression of nucleation time *versus* drop distance from the array center, then multiplying the slope by the cooling rate, there seems to be little correlation between drop position and temperature ($R^2 = 0.033$, average value derived from eight experiments in Fig. 2); any radial temperature gradients within the array were too small to be accurately measured in this study.

From homogeneous nucleation theory, it is possible to infer the temperature-dependent surface energy at the solid–liquid interface, σ , by assuming a spherical crystal nucleus, as:

$$\frac{\partial(\ln J)}{\partial(1/T\Delta T^2)} = -\frac{16\pi\sigma^3 T_m^2}{3\Delta h_f^2 k} \quad (8)$$

where ΔT is the super-cooling ($T_m - T$), Δh_f is the volumetric latent heat of fusion ($3.34 \times 10^8 \text{ J m}^{-3}$ for water at 0°C), and it is assumed that the temperature dependence of ΔG is much greater than for Δg .²⁰ By computing the derivative on the left in eqn (8) numerically (nearly constant in the relevant temperature ranges here), we find σ to be 29.2 mJ m^{-2} for the reference curve for water³² and 33.4 mJ m^{-2} for our data. The surface energy of the ice–water interface was previously measured to be $33 \pm 3 \text{ mJ m}^{-2}$ at 0°C ,³⁶ and σ is predicted to fall with lower temperatures.⁵

In addition to measuring the time and temperature of nucleation for each drop, the dynamics of solidification were also recorded. Typical microscopic images for drops with each of the four concentrations of glycerol are given for times before, during and after freezing in Fig. 3. As crystallization results in a small increase in drop diameter and a sudden brightening of the drop when viewed with crossed-polarization microscopy, the time-course of average image intensity (brightness) within a single

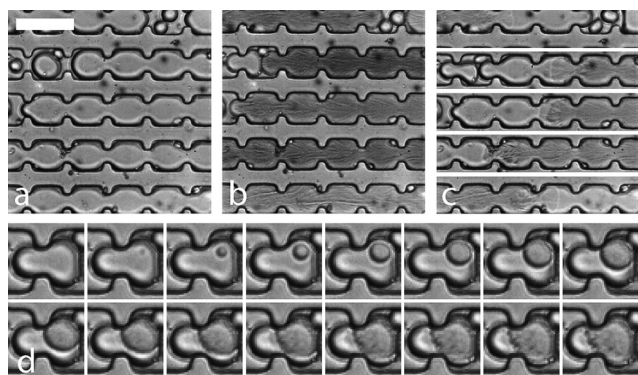


Fig. 4 High-speed imaging of nucleation and solidification in polydisperse drops of 10% w/w glycerol in water. Bright-field image in (a) is from 12.7 seconds after the start of an applied cooling ramp of $1.48\text{ }^{\circ}\text{C s}^{-1}$ after stabilization at $-30\text{ }^{\circ}\text{C}$ (100 μm bar). The image in (b) was taken 1.9 seconds later, by which time all freezing events in ESI video 5 had occurred. Images in (c) show the solid–liquid interface in large drops in each row. Sequential images in (d) of the drop at left in row 2 show the sub-millisecond dynamics just after the nucleation event itself (123 μs between frames, enlarged $2\times$). Here, the emulsion was prepared by mixing a small amount of aqueous phase with surfactant-containing fluorocarbon oil, and a similar array, with spacing of 70 μm between traps in a single channel and 80 μm between channels, was utilized.

drop contains a jump discontinuity at the moment of nucleation (curves on the left in Fig. 3). Fig. 4 uses a similar array to immobilize polydisperse drops, demonstrating how the sub-millisecond dynamics of solidification can be observed with a high speed camera. Here, freezing in each large drop, as well as the details just after the nucleation event inside one smaller drop, were observed. In order of occurrence, the solid–liquid interface was observed to travel with velocities of 2.19, 2.37, 2.44, 2.32 and 2.47 cm s^{-1} for the larger drops, suggesting an increase of 0.10 cm s^{-1} in the velocity of the solid–liquid interface for a $1\text{ }^{\circ}\text{C}$ drop in temperature ($R^2 = 0.81$).

Although stable for pure water drops, significant darkening was observed to occur over several seconds post-nucleation for all drops containing some level of glycerol. This is analogous to darkening observed subsequent to intracellular ice formation in normal cell media³⁷ though not necessarily due to the same physical processes. For the drops containing glycerol, the lower temperatures (nucleation was typically around $-59\text{ }^{\circ}\text{C}$ for drops of 30% w/w glycerol) and higher starting concentration of glycerol imply drops with the highest fluid viscosities of all cases measured. As ice rejects impurities to a high degree, the concentration of glycerol in the remaining unfrozen portion of the drop will increase as freezing proceeds. From the supplemented phase diagram for water–glycerol,³⁸ it is clear that the concentration of glycerol in the fluid at the solid–liquid interface could rise to as much as 72% w/w in the coldest observed temperature window (-61 to $-57.5\text{ }^{\circ}\text{C}$), so the unfrozen fraction is not yet glassy for any case where we observe darkening. Vitrification of the unfrozen fraction would only occur below T_g prime, the temperature where the liquidus line intersects that of the glass transition in the equilibrium phase diagram. This would occur at a temperature of around $-95\text{ }^{\circ}\text{C}$ for the water–glycerol binary system, where the glycerol concentration would rise to about 80% w/w.³⁸ Moreover, the substantial increase in glycerol

concentration within the unfrozen fluid of a nucleated drop should quench any further nucleation events during slow cooling.

If we assume equilibrium is approached only slowly due to the increasingly high viscosity of the unfrozen fraction, the timescale of darkening may be explained as slow growth of ice dendrites due to Mullins–Sekerka instability,³⁹ resulting in a structure that scatters light. On the other hand, if we assume equilibrium is achieved shortly after nucleation, the longer time scale for darkening in the 30% w/w glycerol droplets may result from the increase in the negative slope of the liquidus line in the water–glycerol phase diagram as the concentration of glycerol becomes higher. To understand this, consider first that the glycerol concentration in the unfrozen fluid just after completion of the immediate nucleation-induced solidification will be smallest in the 10% w/w droplets (60% w/w) and largest in the 30% w/w drops (72% w/w). Since the cooling rate is constant, the increasingly negative slope of the liquidus line means that the equilibrium glycerol concentration will increase most slowly for the 30% w/w glycerol starting point. Since the regular array of droplets allows the dynamics of every drop to be preserved, we may discount this second possibility; frozen drops are observed at different stages of darkening at a single temperature, as seen in Fig. 1c. This implies that the drops which had frozen earliest are in fact closer to equilibrium than more recently frozen drops and that diffusion-limited growth of crystals is occurring. Though this implies a dendritic structure consistent with the sub-millisecond dynamics of nucleation and solidification evident in Fig. 4 and the associated high speed video (ESI video 5†), further investigations are warranted. For example, thin sections of frozen drops could be observed *via* transmission electron microscopy, and this would be possible at room temperature if drops were stabilized with freeze-substitution.⁴⁰ If present, it follows that the dendritic crystal structure would scatter incident light in all directions so that only a small fraction would continue vertically and be captured by the camera.

Conclusion

Emulsion studies of nucleation and solidification become more accurate with the use of monodisperse drops. The subsequent immobilization of these drops in an array with regular drop–drop spacing provides new means to simultaneously track an entire thermodynamic excursion in more than 100 drops with single-drop resolution. This controlled geometric arrangement also provides a window to any drop–drop interactions that would otherwise be lost in the average behavior of a bulk emulsion. Moreover, the ability to observe the dynamics of drops that differ only in their time of nucleation should allow for new insights into non-equilibrium thermodynamics. Although we have used low-magnification images to observe a large number of droplets simultaneously, one could obtain more precise information on the freezing process *via* laser scanning confocal microscopy, where fluorescent dye would remain only in the unfrozen fraction of the aqueous drop, yielding geometry and viscosity⁴¹ of the remaining unfrozen fraction in real time, on a drop-by-drop basis.

Acknowledgements

This work was supported by the NIBIB (P41 EB002503), the HFSP (RGP0004/2005-C102), the NSF (DMR-0602684 and

DBI-0649865) and the Harvard MRSEC (DMR-0820484). JFE was supported by an NIH Postdoctoral Fellowship through the NIBIB (F32 EB007901).

References

- 1 D. Kashchiev and G. M. Rosmalen, *Crystal Research and Technology*, 2003, **38**, 555–574.
- 2 A. C. Zettlemoyer, *Nucleation*, Marcel Dekker, New York, 1969.
- 3 J. W. Mullin, *Crystallisation*, Butterworth & Co, London, 1972.
- 4 D. Kashchiev, *Nucleation*, Butterworth–Heinemann, 2000.
- 5 P. V. Hobbs, *Ice Physics*, Oxford University Press, Oxford, UK, 1974.
- 6 D. Turnbull and J. C. Fisher, *Journal of Chemical Physics*, 1949, **17**, 71–73.
- 7 J. B. Zeldovich, *Acta Physicochimica URSS*, 1943, **18**, 1–22.
- 8 A. Laaksonen, V. Talanquer and D. W. Oxtoby, *Annual Reviews in Physical Chemistry*, 1995, **46**, 489–524.
- 9 A. Tabazadeh, Y. S. Djikaev and H. Reiss, *PNAS*, 2002, **99**, 15873–15878.
- 10 M. Griffith and K. V. Ewart, *Biotechnology Advances*, 1995, **13**, 375–402.
- 11 J.-u. Shim, G. Cristobal, D. R. Link, T. Thorsen and S. Fraden, *Crystal Growth & Design*, 2007, **7**, 2192–2194.
- 12 B. Zheng, L. S. Roach and R. F. Ismagilov, *Journal of the American Chemical Society*, 2003, **125**, 11170–11171.
- 13 W. F. Rall and G. M. Fahy, *Nature*, 1985, **313**, 573–575.
- 14 V. Berejnov, N. S. Hussein, O. A. Alsaied and R. E. Thorne, *Journal of Applied Crystallography*, 2006, **39**, 244–251.
- 15 D. Turnbull, *Metallurgical Transactions A—Physical Metallurgy and Materials Science*, 1981, **12**, 695–708.
- 16 G. M. Pound and V. K. La Mer, *Journal of the American Chemical Society*, 1952, **74**, 2323–2332.
- 17 M. L. White and A. A. Frost, *Journal of Colloid Science*, 1959, **14**, 247–251.
- 18 D. Kashchiev, N. Kaneko and K. Sato, *Journal of Colloid and Interface Science*, 1998, **208**, 167–177.
- 19 D. Turnbull, *Journal of Chemical Physics*, 1952, **20**, 411–424.
- 20 M. J. Oliver and P. D. Calvert, *Journal of Crystal Growth*, 1975, **30**, 343–351.
- 21 B. Krämer, O. Hübner, H. Vortisch, L. Wöste, T. Leisner, M. Schwell, E. Rühl and H. Baumgärtel, *Journal of Chemical Physics*, 1999, **111**, 6521–6527.
- 22 T. P. Melia and W. P. Moffitt, *Journal of Colloid Science*, 1964, **19**, 433–447.
- 23 P. Laval, J.-B. Salmon and M. Joanicot, *Journal of Crystal Growth*, 2007, **303**, 622–628.
- 24 S. L. Anna, N. Bontoux and H. A. Stone, *Applied Physics Letters*, 2003, **82**, 364–366.
- 25 C. H. J. Schmitz, A. C. Rowat, S. Köster and D. A. Weitz, *Lab on a Chip*, 2009, **9**, 44–49.
- 26 J. Leng and J.-B. Salmon, *Lab on a Chip*, 2009, **9**, 24–34.
- 27 O. Galkin and P. G. Vekilov, *Journal of Physical Chemistry B*, 1999, **103**, 10965–10971.
- 28 A. S. Utada, A. Fernandez-Nieves, H. A. Stone and D. A. Weitz, *Physical Review Letters*, 2007, **99**, 094502.
- 29 J. Clausell-Tormos, D. Lieber, J.-C. Baret, A. El-Harrak, O. J. Miller, L. Frenz, J. Blouwolff, K. J. Humphry, S. Köster, H. Duan, C. Holtze, D. A. Weitz, A. D. Griffiths and C. A. Merten, *Chemistry & Biology*, 2008, **15**, 427–437.
- 30 C. Holtze, A. C. Rowat, J. J. Agresti, J. B. Hutchison, F. E. Angilè, C. H. J. Schmitz, S. Köster, H. Duan, K. J. Humphry, R. A. Scanga, J. S. Johnson, D. Pisignano and D. A. Weitz, *Lab on a Chip*, 2008, **8**, 1632–1639.
- 31 J. C. McDonald, D. C. Duffy, J. R. Anderson, D. T. Chiu, H. Wu, O. J. A. Schueller and G. M. Whitesides, *Electrophoresis*, 2000, **21**, 27–40.
- 32 P. Stöckel, I. M. Weidinger, H. Baumgärtel and T. Leisner, *Journal of Physical Chemistry A*, 2005, **109**, 2540–2546.
- 33 V. F. Petrenko and R. W. Whitworth, *Physics of Ice*, Oxford University Press, USA, 2002.
- 34 B. J. Mason, *Physics of clouds*, Clarendon Press, Oxford, 1957.
- 35 V. I. Khvorostyanov and J. A. Curry, *Journal of Physical Chemistry A*, 2004, **108**, 11073–11085.
- 36 W. M. Ketcham and P. V. Hobbs, *Philosophical Magazine*, 1969, **19**, 1161–1173.
- 37 S. L. Stott and J. O. M. Karlsson, *Cryobiology*, 2009, **58**, 84–95.
- 38 S. Ablett, M. J. Izzard and P. J. Lillford, *Journal of the Chemical Society, Faraday Transactions*, 1992, **88**, 789–794.
- 39 W. W. Mullins and R. F. Sekerka, *Journal of Applied Physics*, 1963, **34**, 323–329.
- 40 L. Salinas-Flores, S. L. Adams, D. A. Wharton, M. F. Downes and M. H. Lim, *Cryobiology*, 2008, **56**, 28–35.
- 41 A. Aksan, D. Irimia, X. He and M. Toner, *Journal of Applied Physics*, 2006, **99**, 064703.